IEEE Access
Multidisciplinary | Rapid Review | Open Access Journal

Received March 19, 2021, accepted March 27, 2021, date of publication March 31, 2021, date of current version April 12, 2021.

Digital Object Identifier 10.1109/ACCESS.2021.3070018

High-Accuracy On-Site Measurement of Wheel Tread Geometric Parameters by Line-Structured Light Vision Sensor

YUNFENG RAN[1], QIXIN HE[1], QIBO FENG[1,2], AND JIANYING CUI[1]
[1]Key Laboratory of Luminescence and Optical Information, Ministry of Education, Beijing Jiaotong University, Beijing 100044, China
[2]Dongguan Nannar Electronic Technology Company Ltd., Dongguan 523050, China

Corresponding author: Qixin He (heqixin@bjtu.edu.cn)

This work was supported in part by the National Natural Science Foundation of China under Grant 51935002, and in part by the Introduced Innovative Research and Development Team of Dongguan: Train wheelset geometric parameters intelligent testing and entire life-cycle management system development and industrial application innovative research team under Grant 201536000600028.

ABSTRACT Railway wheels are one of the important parts of railway vehicles, and it is necessary to inspect their status frequently. To measure the wheel tread geometric parameters dynamically and accurately in a train running environment, a line-structured light vision sensor-based measurement system was demonstrated in this paper. In the system, a subpixel laser stripe centre extraction algorithm based on skeleton extraction, which can significantly reduce the interference of complex lighting environments in the field and greatly improve the extraction accuracy, was proposed. To further improve the measurement accuracy and stability, the influence of the eccentricity error caused by the dynamic measurement on the results was analyzed, a mathematical model was established, and the deformed profile was corrected. The system has been successfully applied to railway maintenance sections and has become a part of train safety inspection systems. Field tests were conducted to verify the performance of the system, and the results showed that the measurement accuracy and stability are marked improved after eccentric error correction, especially for the flange height and QR value.

INDEX TERMS Sensor systems and applications, railway safety, measurement.

I. INTRODUCTION

With the continuous development of railway transportation, train speeds are increasing, and the timely safety inspection of trains and rails is becoming increasingly important [1]. In recent years, the automatic safety inspection of key components of trains and tracks, such as bogie block keys [2], axle bearings [3]–[5], split pins [6], train bottoms [7], track gauges [8] and carbon contact strips [9], has been achieved on site. Accurate and regular measurement of the wheel size, including the wheel diameter and tread geometric parameters, is one of the most important means for avoiding overturned trains and providing safety assurance, which has become a high-priority issue for researchers [10]–[13]. With the development of image processing technology such as characteristic extraction, feature matching and imaging mosaics [14], [15], line-structured light vision sensors have become a commonly used method for the on-site measurement of wheel tread profiles. Verities of applications of structured light vision for precise wheel size measurement have been described in [16]–[23]. For example, Pan [16] used two identical structured-light vision sensors measuring one wheel each and fused the profile data to reduce leak and false-positive rates. Xing [17] arranged two coplanar 2-D laser displacement sensors (2D-LDSs) inside and outside the railway to measure the wheel tread profile. In addition, two extra 2D-LDSs were arranged to measure the wheel diameter by the three-point fitting method. Cheng [18] replaced one of the 2D-LDSs with a 1D-LDS to obtain a higher measurement accuracy and lower costs. Since the measurement frequency of 2D-LDSs is much lower than that of 1D-LDSs, a very low speed while the train passes the sensors is required to obtain a good wheel diameter result. Chen [19] applied a similar configuration as our system and discussed different types of measurement errors, and the measurement accuracy is about 0.18 mm. Pan [20] established a quality evaluation

The associate editor coordinating the review of this manuscript and approving it for publication was Chunsheng Zhu.

This work is licensed under a Creative Commons Attribution-NonCommercial-NoDerivatives 4.0 License.
For more information, see https://creativecommons.org/licenses/by-nc-nd/4.0/

criterion of stripe images and divided the images into different types of segments. In addition, the low-brightness segments were enhanced according to multiscale Retinex theory, which improved the reliability of stripe extraction. Soleimani [21] provided an applied method for measuring the railway wheel profile with photographing from the railway wheel to measure by image processing techniques. The measurement results were compared with Calipri laser device that results in acceptable achievements. These systems have achieved good results in indoor and static environments, but the accuracy tends to decline in field environments. The main reasons are as follows: (1) In field applications, due to the complex background environment and specific shape of wheels, laser stripes have different widths and brightnesses, and the grey distribution of the light stripe does not conform to a Gaussian function. In addition, bright spots and stripe cracks will occur due to the different reflectivities of wheel surfaces. These factors increase the difficulty of strip centre extraction, resulting in the poor performance of existing strip centre extraction algorithms, such as the grey gradient method [24], Gaussian fitting [25], the Canny operator [26], Kalman filtering [27], the Steger method [28] and multi-scale extraction algorithm [29], which will increase the missed detection rate and false alarm rate of a system. (2) The influence of the eccentricity error on the measurement results in a dynamic measurement environment need to be considered. In a wheel tread profile on-site measurement system, the measurement position of the wheel is determined by the trigger position, which is related to the radius of the wheel. Different wheel diameters will lead to different measurement positions, resulting in a distance between the laser plane of the sensor and the centre of the wheel, which is called the eccentricity error. Due to the eccentricity error, the laser profile of the measured wheel will be deformed, and the measurement error will increase.

To achieve high-accuracy on-site detection of wheel tread geometric parameters, a line-structured light vision sensor-based measurement system is demonstrated in this paper, and the above issues in field measurement are solved. First, a subpixel laser stripe centre extraction algorithm based on skeleton extraction, which can significantly reduce the interference of complex lighting environments in the field and greatly improve the extraction accuracy and reliability, is proposed. Second, the influence of the eccentricity error caused by dynamic measurement is analyzed, the mathematical model is established, and the deformed profile is corrected. Finally, field experiments are conducted at railway sites, the correctness of the eccentricity error modification model is verified, and the performance of the system is evaluated based on the results of the experiments. After correction, the reliability and repeatability of the system are significantly improved, especially for the flange height and QR value.

The remainder of this paper consists of four parts. First, in Section 2, the detection procedure and system structure are described. The subpixel laser stripe centre extraction algorithm and its effects are described in Section 3. In Section 4, the influencing factors of the eccentricity error are analyzed, and the measurement results are corrected. In Section 5, field experiments are conducted, and the system performance is evaluated.

II. SYSTEM PRINCIPLE AND CONFIGURATION

The definitions of the typical tread profile parameters are shown in Fig. 1. The point with a horizontal distance of 70 mm from the inside surface is set as the datum point. Reference point A is defined as the point on the flange 12 mm above the datum point. The flange height (FH) is defined as the longitudinal distance between the vertex point of the flange and the datum point, which reflects the tread wear. The flange thickness (FT) is defined as the horizontal distance between reference point A and the inside surface. Reference point B is defined as the point on the flange 2 mm lower than the vertex point of the flange. The QR value is defined as the horizontal distance between reference points A and B.

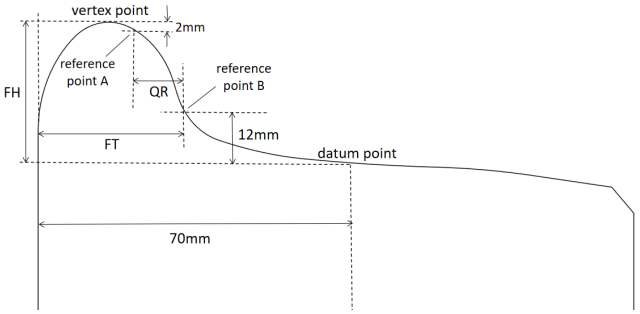

FIGURE 1. Definitions of wheel tread profile geometric parameters. FH: flange height; FT: flange thickness.

The system consists of three modules: a sensor module, a data processing module and a data storage module. The sensor module is mainly composed of line structured light sensors, photoelectric switches, magnetic steel switches and their respective accessories, as shown in Fig. 2 (a).

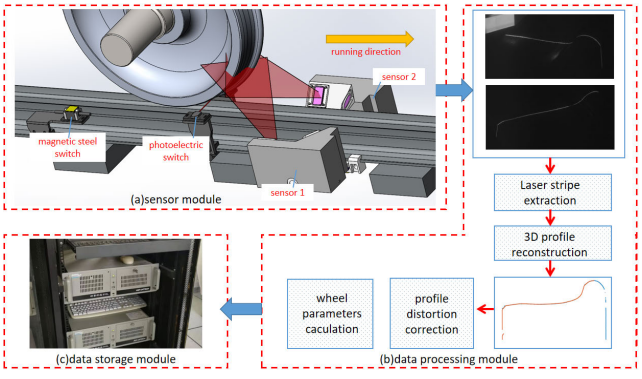

FIGURE 2. Schematic of the system.

The magnetic steel switch and the photoelectric switch are mounted before the linear structured light sensors. When the train passes, the magnetic steel switch generates a trigger signal to wake up the measurement system. The photoelectric

switches emit a synchronous signal to light the laser and trigger the camera to capture images when the wheel flange blocks the infrared ray. Then, the images are transmitted to the data processing module and processed to extract the laser stripes. Three-dimensional reconstruction of the tread profile is conducted according to the calibration parameters, as shown in Fig. 2 (b). Finally, the profile deformation caused by the eccentricity error is corrected, and the tread parameters are calculated according to the corrected tread profile.

In the system, four line-structured light sensors are mounted on the two sides of each rail to measure the profile of the wheel tread. The inner and outer laser planes of the two sensors around the measured wheel are adjusted to be coplanar in space and then fixed. The parameters of the linear structured light sensor are specially designed according to the wheel shape. The pixel size of the camera is 4.4 μm * 4.4 μm, and the focal length of the lens is 12 mm. The system can reach 0.11 mm theoretical measurement accuracy at the designed 300 mm work distance. The minimum exposure time of the camera used was 25 μs. The exposure process will widen the laser line. Considering that the acceptable increment of the laser line width is 0.1 mm, the maximum train speed is approximately 20.3 km/h. The maximum frame rate of the camera is 200 fps, which meets the requirements of the on-site dynamic measurement of wheel tread parameters. The total cost of the system including the sensor module, data processing module and data storage module is under fifty thousand yuan.

To overcome the difficulties of field calibration, the system adopts a specially designed calibration device, which can complete the entire calibration process in only one shot. The calibration device is composed of a magnetic base, an adjustable bracket composed of multiple cardan joints and a calibration plate, as shown in Fig. 3. During the calibration, the magnetic base is fixed on the rail, and the plane of the calibration plate is carefully adjusted to coincide with the laser plane through the bracket and put it in a suitable position in the camera view. Then, the image of the calibration plate is obtained, and the pixel coordinates of the corner points on the plate are extracted. The plane coordinates of the calibration plate were determined when the calibration plate was manufactured. Since the laser plane coincides with the calibration plate plane, it can be considered that the coordinate of the laser plane is equal to the coordinate of the calibration plate plane. The functional relationship between the laser plane coordinates (L_{xi}, L_{yi}) and the pixel coordinates (u_i, v_i) can be obtained by the following polynomial fitting method:

$$L_{xi} = k_0 + k_1 u_i + k_2 v_i + k_3 u_i^2 + k_4 u_i v_i + k_5 v_i^2 + \cdots \quad (1)$$

$$L_{yi} = n_0 + n_1 u_i + n_2 v_i + n_3 u_i^2 + n_4 u_i v_i + n_5 v_i^2 + \cdots \quad (2)$$

Assuming that the number of corner points is m and the number of terms of the polynomial is q, when q<m, the coefficients of the polynomial can be solved by the following overdetermined equations:

$$Qt = L \quad (3)$$

where

$$Q = \begin{bmatrix} 1 & u_1 & v_1 & \cdots \\ \cdots & \cdots & \cdots & \cdots \\ 1 & u_m & v_m & \cdots \end{bmatrix} t = \begin{bmatrix} k_0 \\ \cdots \\ k_q \end{bmatrix} or \begin{bmatrix} n_0 \\ \cdots \\ n_q \end{bmatrix}$$

$$L = \begin{bmatrix} L_{x1} \\ \cdots \\ L_{xm} \end{bmatrix} or \begin{bmatrix} L_{y1} \\ \cdots \\ L_{ym} \end{bmatrix}$$

The overdetermined equations have unique least square solutions:

$$t = (Q^T Q)^{-1} Q^T L \quad (4)$$

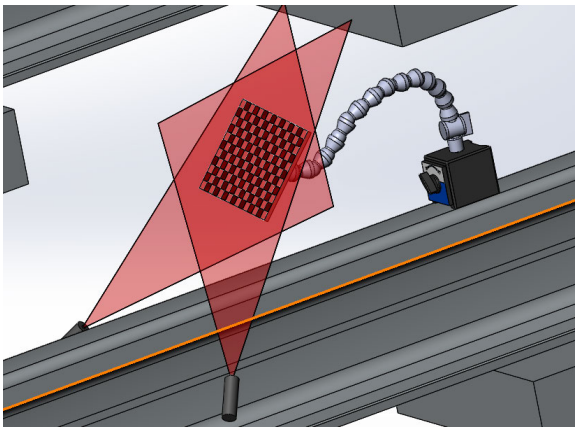

FIGURE 3. Schematic diagram of the calibration process.

III. SUBPIXEL EXTRACTION OF THE LASER STRIPE IN A COMPLEX BACKGROUND

The extraction of the laser stripe centre is an important factor affecting the accuracy of structured light measurement. To achieve high-accuracy and high reliability extraction of laser stripe centres, a subpixel extraction algorithm based on skeleton extraction that is suitable for field tests is proposed. The method can be divided into three steps: laser stripe segmentation, skeleton extraction and subpixel accuracy extraction of the laser stripe centre.

A. LASER STRIPE SEGMENTATION

Laser stripe segmentation is an initial and important step in the laser stripe centre extraction process that directly determines the extraction effect. The purpose of laser stripe segmentation is to divide the original image into the foreground region containing laser stripes and the background region. A good segmentation algorithm can eliminate the interference caused by stray light, an uneven brightness of laser stripes and an uneven width of laser stripes. Previous works on point feature recognition such as [14] and [15] are instructive to the segment process, which can help to distinguish the real laser stripe and stray light. In this paper, a segmentation algorithm combining the self-difference method, the directional template method and the morphological operation is

proposed; and the algorithm can achieve good results even under complex illumination conditions.

The self-difference procedure is applied to eliminate the influence of the uneven brightness of laser stripes in the original image. In this process, the original image is filtered, and then the difference image is obtained by subtracting the filtered image from the original image. Finally, pixels with a grey value greater than that of the surrounding area are selected by threshold segmentation of the difference image. The stripe images after self-difference are shown in the second column of Fig. 4.

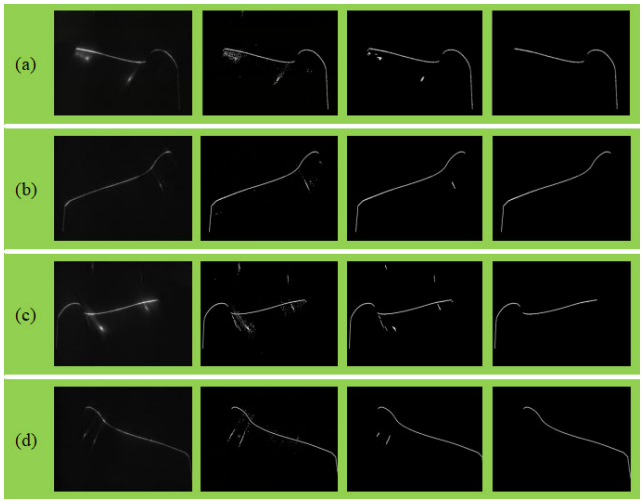

FIGURE 4. The process of the laser stripe segmentation algorithm for four different actual images: the first column is the original images, the second column is the self-difference results, the third column is the direction template method results, and the fourth column is the shape operation results.

The directional template method is used to further eliminate the interference of ambient light based on the Gaussian distribution characteristics of the laser stripe intensity. In this method, the direction template shown in Table 1 is used to convolve the original image, and then the pixels with the maximum values in the direction of the convolution template are selected from the convolved image. The stripe images processed by the directional template method are shown in the third column of Fig. 4.

Finally, the small branches besides the backbone of the laser stripe are removed by the morphological operation, as shown in the fourth column of Fig. 4.

B. SKELETON EXTRACTION OF LASER STRIPES

After laser stripe segmentation, a binary image B_0 is obtained, and the next step is to obtain the stripe skeleton from B_0. The Zhang fast parallel thinning algorithm [30] is a commonly used algorithm to obtain binary image skeletons. This algorithm can accurately maintain the characteristics of straight lines and corners and has a fast processing speed due to the fewer number of iterations.

For the 8-neighbour system shown in Fig. 5, the steps of the Zhang parallel thinning algorithm are as follows:

Zhang Parallel Thinning Algorithm

Input: Laser stripe segmentation binary image B_0
Output: Laser stripe skeleton binary image S_0
Step 1: Delete the boundary points satisfying the following conditions:
① $2 \le N(P1) \le 6$ ② $S(P1) = 1$ ③ $P2*P4*P6 = 0$ ④ $P4*P6*P8 = 0$.
Step 2: Delete the boundary points satisfying the following conditions:
① $2 \le N(P1) \le 6$ ② $S(P1) = 1$ ③ $P2*P4*P8 = 0$ ④ $P2*P6*P8 = 0$.
Step 3: Repeat steps 1 and 2 until no boundary points can be deleted.

TABLE 1. The used direction template.

0° ,
$$\begin{bmatrix} 0.14 & 0.14 & 0.14 & 0.14 & 0.14 \\ 0.61 & 0.61 & 0.61 & 0.61 & 0.61 \\ 1 & 1 & 1 & 1 & 1 \\ 0.61 & 0.61 & 0.61 & 0.61 & 0.61 \\ 0.14 & 0.14 & 0.14 & 0.14 & 0.14 \end{bmatrix}$$

22.5° ,
$$\begin{bmatrix} 0.56 & 0.34 & 0.18 & 0.08 & 0.03 \\ 0.99 & 0.86 & 0.65 & 0.43 & 0.24 \\ 0.75 & 0.93 & 1 & 0.93 & 0.75 \\ 0.24 & 0.43 & 0.65 & 0.86 & 0.99 \\ 0.03 & 0.08 & 0.18 & 0.34 & 0.56 \end{bmatrix}$$

45° ,
$$\begin{bmatrix} 1 & 0.78 & 0.37 & 0.11 & 0.02 \\ 0.78 & 1 & 0.78 & 0.37 & 0.11 \\ 0.37 & 0.78 & 1 & 0.78 & 0.37 \\ 0.11 & 0.37 & 0.78 & 1 & 0.78 \\ 0.02 & 0.11 & 0.37 & 0.78 & 1 \end{bmatrix}$$

67.5° ,
$$\begin{bmatrix} 0.56 & 0.99 & 0.75 & 0.24 & 0.03 \\ 0.34 & 0.86 & 0.93 & 0.43 & 0.08 \\ 0.18 & 0.65 & 1 & 0.65 & 0.18 \\ 0.08 & 0.43 & 0.93 & 0.86 & 0.34 \\ 0.03 & 0.24 & 0.75 & 0.99 & 0.56 \end{bmatrix}$$

90° ,
$$\begin{bmatrix} 0.14 & 0.61 & 1 & 0.61 & 0.14 \\ 0.14 & 0.61 & 1 & 0.61 & 0.14 \\ 0.14 & 0.61 & 1 & 0.61 & 0.14 \\ 0.14 & 0.61 & 1 & 0.61 & 0.14 \\ 0.14 & 0.61 & 1 & 0.61 & 0.14 \end{bmatrix}$$

112.5° ,
$$\begin{bmatrix} 0.03 & 0.24 & 0.75 & 0.99 & 0.56 \\ 0.08 & 0.43 & 0.93 & 0.86 & 0.34 \\ 0.18 & 0.65 & 1 & 0.65 & 0.18 \\ 0.34 & 0.86 & 0.93 & 0.43 & 0.08 \\ 0.56 & 0.99 & 0.75 & 0.24 & 0.03 \end{bmatrix}$$

135° ,
$$\begin{bmatrix} 0.02 & 0.11 & 0.37 & 0.78 & 1 \\ 0.11 & 0.37 & 0.78 & 1 & 0.78 \\ 0.37 & 0.78 & 1 & 0.78 & 0.37 \\ 0.78 & 1 & 0.78 & 0.37 & 0.11 \\ 1 & 0.78 & 0.37 & 0.11 & 0.02 \end{bmatrix}$$

157.5° ,
$$\begin{bmatrix} 0.03 & 0.24 & 0.18 & 0.34 & 0.56 \\ 0.24 & 0.43 & 0.65 & 0.86 & 0.99 \\ 0.75 & 0.93 & 1 & 0.93 & 0.75 \\ 0.99 & 0.86 & 0.65 & 0.43 & 0.24 \\ 0.56 & 0.34 & 0.18 & 0.08 & 0.03 \end{bmatrix}$$

P9	P2	P3
P8	P1	P4
P7	P6	P5

FIGURE 5. The definition of the points in an 8-neighbour system.

In the algorithm, N (P1) represents the number of nonzero points in P2, P3, . . ., P9; and S(P1) is the number of changes from 0 to 1 in P2, P3, . . ., P9. The processing results of the Zhang parallel thinning algorithm are shown in Fig. 6.

Some small branches still exist in the skeleton image obtained after thinning algorithm processing, which will affect the accuracy of subsequent processing, as shown in Fig. 7. The next step is to eliminate these small branches and extract the main skeleton.

The steps to extract the skeleton backbone are as follows.

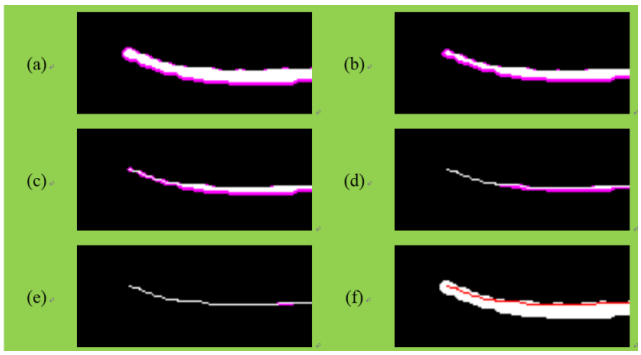

FIGURE 6. The running process of the Zhang parallel thinning algorithm for local images. (a) ∼ (e): Iterative process and (f): the skeleton extraction result.

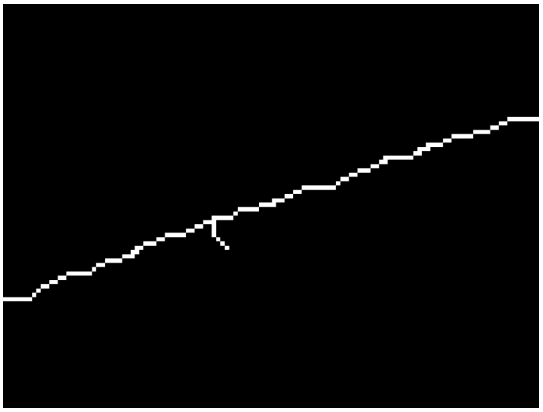

FIGURE 7. The small branches in the laser stripe skeleton.

Laser Stripe Backbone Extraction Algorithm

Input: Laser stripe skeleton binary image S_0
Output: Laser stripe main skeleton binary image S_1
Step 1: Find all endpoints in S_0 and classify the connected endpoints as different sets.
Step 2: Starting from any endpoint in a set (assuming that the endpoint is A), calculate the path from A to the remaining endpoints in the set.
Step 3: Find the endpoint that has the longest distance from endpoint A (assuming that the endpoint is B), and calculate the distance from B to the remainder of the endpoints in the set. Then, find the endpoint that has the longest distance from endpoint B (assuming that the endpoint is C). The path between B and C is the main skeleton without branch.
Step 4: Repeat steps 2 and 3 for all collections to get the complete main skeleton.

C. SUBPIXEL CENTRE EXTRACTION OF LASER STRIPES

The main skeleton binary image obtained after skeleton extraction deviates from the centre of the laser stripe, as shown in Fig. 6 (f). Therefore, it is necessary to further process the main skeleton of laser stripes. In this procedure, the main skeleton extracted in the last step is used as the initial point of subpixel extraction. The normal vector of the main skeleton points is calculated by polynomial fitting of points nearby. The subpixel laser stripe centre can be obtained by calculating the square weighted centre of the grey value of each main skeleton point according to the direction of its normal vector.

The square weighted centre of gravity is calculated according to the direction of the normal vector, which can represent the subpixel centre of the laser stripes:

$$u_s = \frac{\sum_{d<D} w_i(d) u_i G_i^2}{\sum_{d<D} w_i(d) G_i^2}, \quad v_s = \frac{\sum_{d<D} w_i(d) v_i G_i^2}{\sum_{d<D} w_i(d) G_i^2} \tag{5}$$

where G_i represents the grey value. $W_i(d)$ represents the weight value, which can be expressed as:

$$W_i(d) = \exp(-\frac{d^2}{2\sigma^2}) \tag{6}$$

Examples of subpixel laser stripe centre extraction results are shown in Fig. 8. The red points represent the main skeleton of the laser stripe, the green lines represent the calculated normal vector of the main skeleton points, and the yellow points represent the subpixel precision extraction results.

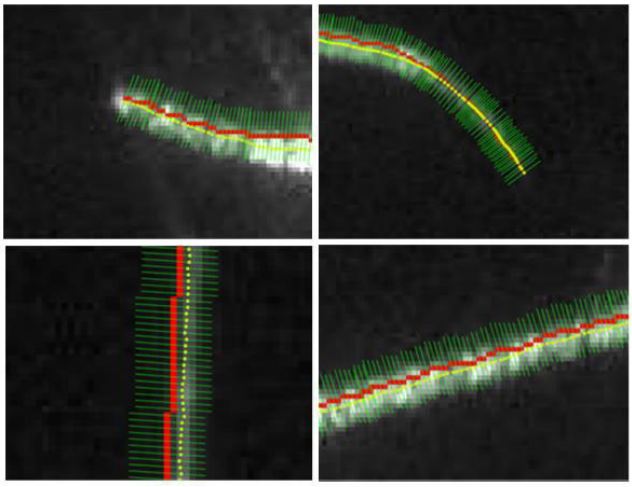

FIGURE 8. Laser stripe centre extraction results: the red points represent the main skeleton of the laser stripe, and the yellow points represent the subpixel precision extraction results.

D. ACCURACY EVALUATION OF THE PROPOSED METHOD

To evaluate the performance of the proposed laser stripe extraction algorithm, stripe centre extraction experiments were conducted on the simulated laser fringe images by our proposed algorithm, the traditional Steger algorithm and the template matching method. The extraction results are shown in Fig. 9, and the comparison is shown in Table 1. Fig. 9(a) and Fig. 9(b) show the two different shapes of the simulated light stripe image. Fig. 9(c) and Fig. 9(d) show the extraction results. The blue dots, red dots and green dots represent the extraction results of our proposed algorithm, the Steger algorithm and the template matching method, respectively.

TABLE 2. The measurement results for a real train.

Method	Proposed		Steger		Template Matching	
Simulated Image	Line	Circle	Line	Circle	Line	Circle
MAE(pixel)	0.159	0.141	0.079	0.387	0.116	0.361
Running Time(s)	0.354	1.118	1.168	2.098	0.574	1.662

MAE: mean absolute error.

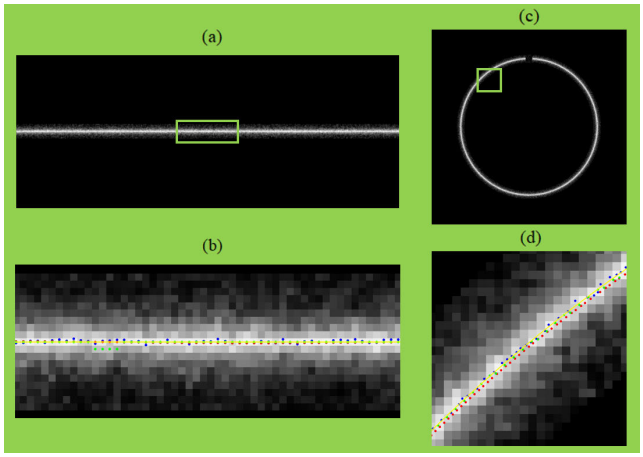

FIGURE 9. Extraction results of simulated laser stripe images. The blue dots, red dots and green dots represent the extraction results of our proposed algorithm, the Steger algorithm and the template matching method, respectively. The yellow dots represent the theoretical stripe centres.

The yellow dots represent the theoretical stripe centre. The Steger algorithm and template matching method perform well on-line images. The mean absolute errors (MAEs) of these two methods are 0.079 pixel and 0.116 pixel, respectively. However, for the circle images, the MAEs reach 0.387 pixel and 0.361 pixel, respectively. The MAEs of our proposed algorithm are 0.159 pixel and 0.141 pixel for the line images and circle images, respectively. That is, our proposed algorithm is better than the other algorithms at handling curved laser stripes, which is important to wheel size measurement. The running time of our proposed algorithm is less than that of the Steger algorithm and template matching method, which is helpful for dynamic measurement.

The measurement accuracy of wheel size corresponding to different stripe image extraction methods was determined. Stripe centre extraction experiments were conducted on real wheel tread images by our proposed algorithm, the traditional Steger algorithm and the template matching method.

The extraction results are shown in Fig. 10. It can be seen that the proposed method has a strong anti-interference ability while the Steger method and template matching method are affected by stray light and ignore many low-brightness regions. The average running time per image for the proposed method is 1.768 s, which is less than the running time of template matching (3.264 s) and of the Steger method (5.795 s).

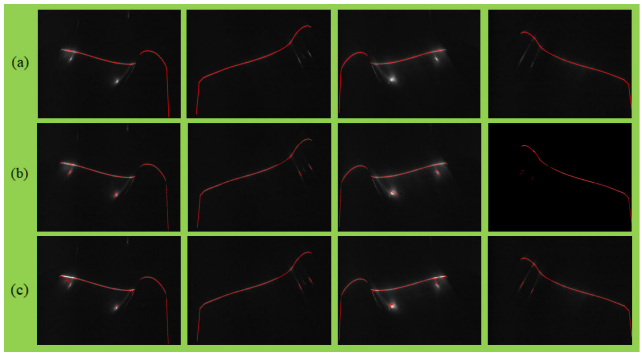

FIGURE 10. Extraction results of four real wheel tread images. (a) Proposed method, (b) Steger method, and (c) template matching method.

Repeatability tests of different stripe extraction methods were also conducted on the same wheel, as shown in Table 2. In the experiments, the stray light was removed artificially, as it could not be removed by the traditional Steger method and template matching method, which affects the calculation of the wheel size. All wheel size results were processed by the same correction process. The variation and root mean square error of the proposed method are less than those of the other two methods. The experimental results show that the extraction method has the advantages of good repeatability in dynamic wheel size measurement.

IV. THE CORRECTION OF THE DISTORTED WHEEL TREAD PROFILE

Wheels can be seen as parallel concentric circles with different diameters, and the laser profile obtained by the sensor is composed of the intersection of the laser plane and these circles. Under ideal conditions, the laser plane OA_1 passes through the centre of the circles and intersects with circles Or_1 and Or_2 at points A_1 and B_1, respectively, as shown in Fig. 11. The height difference observed by the reconstructed wheel tread profile $d_1 = \overline{A_1B_1} = r_2 - r_1$ is equal to the radius difference, which means that the reconstructed wheel tread profile has no distortion.

In the on-site dynamic measurement of the wheel tread profile, due to the different measurement positions caused by different wheel diameters and wheel tread abrasion, the laser plane will deviate from the centre of the circles and intersect with the tread profile at points A_2 and B_2. In this case, the height difference $d_2 = \overline{A_2B_2}$ can be expressed as:

$$d_2 = \sqrt{r_2^2 - e^2} - \sqrt{r_1^2 - e^2} \tag{7}$$

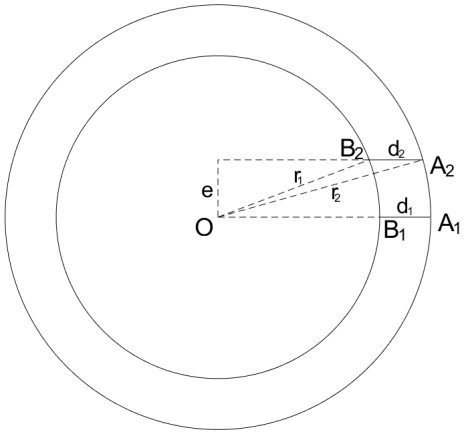

FIGURE 11. Schematic of profile distortion caused by eccentricity error.

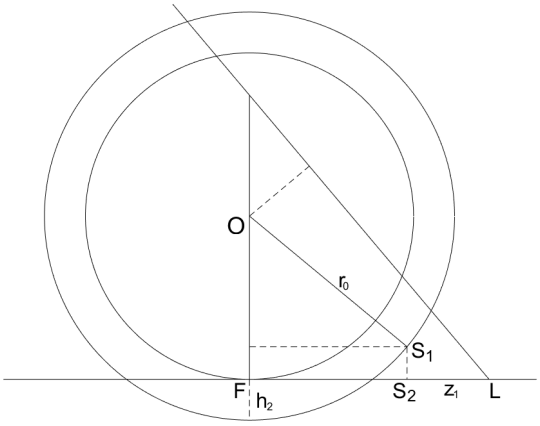

FIGURE 12. Schematic of the wheel position when the photoelectric switch triggers.

where e represents the eccentricity error. The ratio of d_1 to d_2 can be expressed as:

$$\begin{aligned}\frac{d_1}{d_2} &= \frac{r_2 - r_1}{\sqrt{r_2^2 - e^2} - \sqrt{r_1^2 - e^2}} \\ &= \frac{(r_2 - r_1)(\sqrt{r_2^2 - e^2} + \sqrt{r_1^2 - e^2})}{r_2^2 - r_1^2} \\ &= \frac{\sqrt{r_2^2 - e^2} + \sqrt{r_1^2 - e^2}}{r_2 + r_1}\end{aligned} \tag{8}$$

Since $r_1 \approx r_2$ and $r_1, r_2 >> e$, we can use a two-step approximation:

$$\frac{d_1}{d_2} = \delta \approx \frac{2\sqrt{r_1^2 - e^2}}{2r_1} \approx 1 - \frac{e^2}{2r_1^2} \tag{9}$$

That is, when $e \neq 0$, the reconstructed wheel tread profile is stretched evenly compared to the real wheel tread profile. To obtain the real wheel tread profile, the reconstructed wheel tread profile needs to be compressed by a compressional factor $\delta = 1 - \frac{e^2}{2r_1^2}$, which is determined by the wheel radius and eccentricity error.

Generally, the radii of train wheels are measured manually after running three months, and the measurement results are stored in a database. Therefore, the wheel radius can be acquired from the database and used as the true diameter for correction as r_1, and the key problem is how to obtain e.

Fig. 12 shows the trigger process of the photoelectric switch. Point F represents the contact point of the wheel and rail, S_1S_2 represents the photoelectric switch, the switch height is $\overline{S_1S_2} = h_1$, L is the laser emitting point, and the flange vertex triggers the photoelectric switch at S_1. The horizontal distance between the photoelectric switch and the laser emitting point is $\overline{S_2L} = z_1$, and the angle of the laser plane is α. For a standard wheel, the radius of the flange vertex is $\overline{OS_1} = r_0 = 447$mm, and the standard flange height is $h_2 = 27$ mm. It can be obtained from the geometric relationship that:

$$e_0 = \left|\sin\alpha(\sqrt{r_0^2 - (r_0 - h_1 - h_2)^2} + z_1) - \cos\alpha(r_0 - h_2)\right| \tag{10}$$

For nonstandard wheels, the radius decreases and the flange height increases because of abrasion:

$$r_0' = r_0 + \Delta r_0, h_2' = h_2 + \Delta h_2 (r_0 \gg h_1, h_2, \Delta r_0 \gg \Delta h_2) \tag{11}$$

The eccentricity error of a nonstandard wheel can be expressed as:

$$e = e\,|_0 + c_{k1}\Delta r_0 + c_{k2}\Delta h_2\,| \tag{12}$$

where

$$\begin{aligned}c_{k_1} &= \frac{(h_1 + h_2)\sin\alpha}{\sqrt{2r_0(h_1 + h_2) - (h_1 + h_2)^2}} - \cos\alpha \\ c_{k_2} &= \frac{(r_0 - h_1 - h_2)\sin\alpha}{\sqrt{2r_0(h_1 + h_2) - (h_1 + h_2)^2}} + \cos\alpha\end{aligned} \tag{13}$$

As we can see from (10), the eccentricity error e varies linearly with the wheel radius and wheel tread abrasion Δh_2. The coefficient of variation and the initial value are determined by the installation parameters h_1, z_1, and a. Since it is difficult to obtain the correct Δh_2 from a distortional wheel tread profile, an iterative method is used to correct the profile in practical applications. First, Δh_2 is calculated according to the distortional profile, and then the profile is corrected by the calculated Δh_2. These two steps are iterative until the results change slightly, as shown in Fig. 13. The first Δh_2 is calculated according to the distortional profile, and r_0 is acquired from the database. Then, e is calculated by (10). After e is obtained, the profile is compressed by the coefficient that is computed by (4). For simplicity, r_1 could be approximately equal to r_0. The correction process is iterative until e changes slightly.

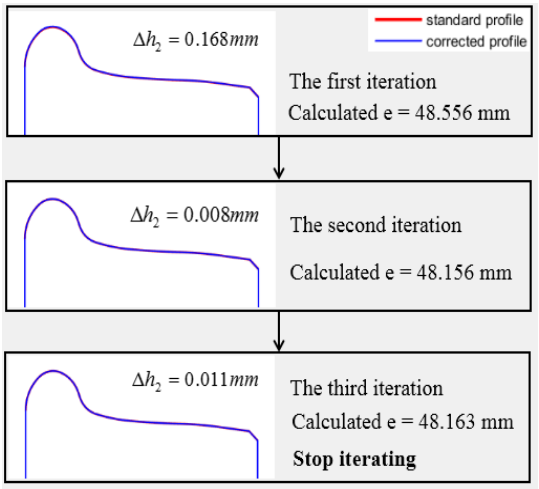

FIGURE 13. The iterative process of profile correction.

V. EXPERIMENTS AND EVALUATIONS

To verify the effectiveness of the sensor system, a line-structured light vision sensor-based wheel tread geometric parameter measurement system was mounted at railway sites, and on-site field tests were performed in Yinchuan, China on November 8, 2020. The system was installed in the garage entrance, and the on-site installation of the sensor is shown in Fig. 14.

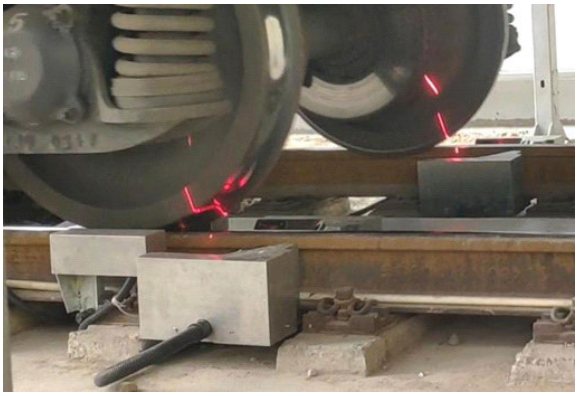

FIGURE 14. On-site measurement system installed for the field test.

Repeated measurements of a real train wheel were conducted. The test was conducted 6 times, and the measurement results of the system before and after correction are shown in Table 4. The table shows that the measurement system has good stability and repeatability before correction. After correction, the stability and repeatability of the system changed little because for a wheel with a certain radius and tread wear, the system will perform the same correction procedure. That is, the correction process will not affect the stability and repeatability of the system for the repeated measurement of a single wheel. The manual measurement results of this wheel by the fourth wheel checker are shown in the last column of Table 4. As for the flange height and QR value, the mean value

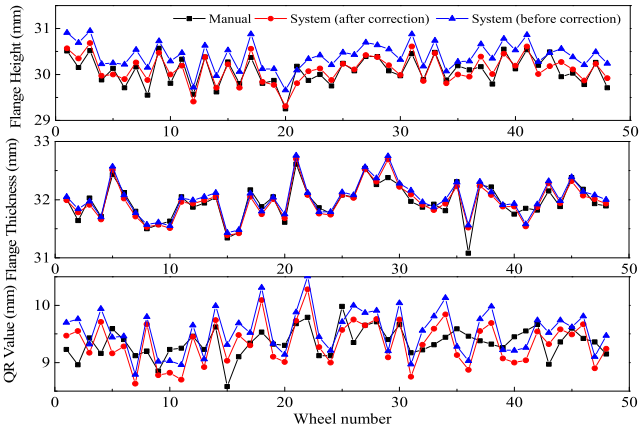

FIGURE 15. Measurement results for the 48 wheels of a real train.

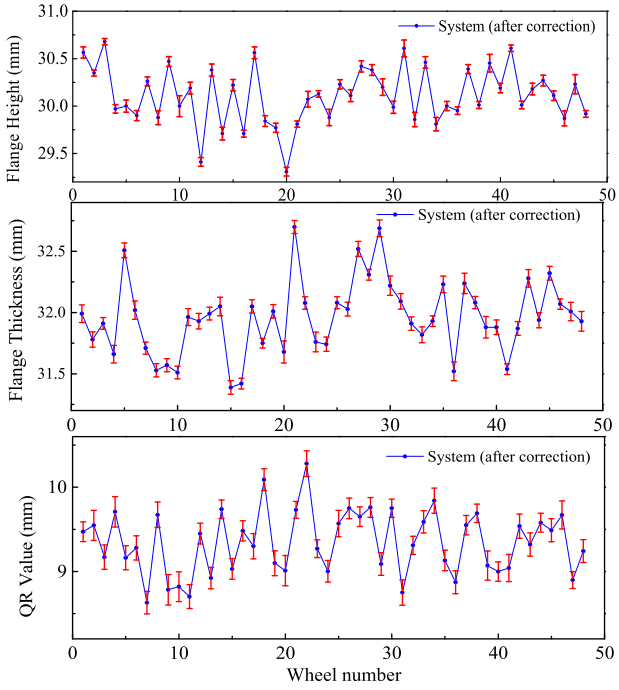

FIGURE 16. The error bars for the system measurement results of a real train.

is closer to the manual measurement value after correction, indicating that the measurement error is reduced after correction.

Measurements of all 48 wheels of a real train were conducted. The geometric sizes of the 48 different wheels were measured manually and by the system. The measurement results are plotted as shown in Fig. 15. The black dots represent the average of 3 manual measurements, the blue dots represent the measurements made by the system without correction of the eccentricity error, and the red dots represent the measurement results after the correction of the eccentricity error. Each point is the average of six measurements.

The statistical analysis of the 48 wheel measurements is shown in Table 5. For the flange height, the mean absolute

TABLE 3. The measurement results for a real wheel.

Measurement Time	Proposed			Steger			Template Matching		
	FH	FT	QR	FH	FT	QR	FH	FT	QR
1	30.53	32.01	9.35	30.57	32.00	9.43	30.51	32.04	9.38
2	30.54	31.91	9.62	30.53	31.87	9.72	30.56	31.92	9.62
3	30.62	32.04	9.57	30.61	32.05	9.58	30.61	32.02	9.58
4	30.65	32.03	9.48	30.67	31.99	9.41	30.72	32.01	9.44
5	30.58	31.88	9.52	30.65	31.87	9.45	30.56	31.86	9.57
6	30.47	32.08	9.29	30.48	32.08	9.25	30.52	32.04	9.23
Mean	30.57	31.99	9.47	30.59	31.98	9.48	30.58	31.98	9.47
Var	0.18	0.20	0.33	0.19	0.21	0.47	0.21	0.18	0.39
RMSE	0.081	0.074	0.268	0.100	0.088	0.284	0.099	0.074	0.276

Var. : variance, RMSE: root mean square error.

TABLE 4. The measurement results for a real wheel.

Measurement time	Flange Height (mm)		Flange Thickness (mm)		QR value (mm)	
	before correction	after correction	before correction	after correction	before correction	after correction
1	30.75	30.53	32.05	32.01	9.54	9.35
2	30.78	30.54	31.95	31.91	9.82	9.62
3	30.85	30.62	32.07	32.04	9.73	9.57
4	30.89	30.65	32.01	32.03	9.58	9.48
5	30.80	30.58	31.93	31.88	9.71	9.52
6	30.68	30.47	32.12	32.08	9.47	9.29
Mean	30.79	30.57	32.02	31.99	9.64	9.47
Var.	0.21	0.18	0.19	0.20	0.35	0.33
RMSE	0.290	0.081	0.067	0.074	0.429	0.268
Manual measurement	30.51		32.01		9.23	

Var. : variance, RMSE: root mean square error.

TABLE 5. The measurement results for a real train.

Results	Flange Height (mm)		Flange Thickness (mm)		QR value (mm)	
	before correction	after correction	before correction	after correction	before correction	after correction
Mean error	0.35	0.14	0.11	0.10	0.31	0.24
Max error	0.66	0.36	0.49	0.44	0.82	0.55
RMSE	0.364	0.154	0.133	0.118	0.408	0.343

RMSE: root mean square error.

error between the system measurement and manual measurement is 0.35 mm, which is reduced to 0.14 mm after correction. The maximum error is calculated to be 0.66 mm, which is reduced to 0.36 mm after correction. The root mean square error is calculated to be 0.364 mm, which is reduced to 0.154 mm after correction. As for the flange thickness, the difference between the initial measurement results and corrected measurement results is small, indicating that the measurement accuracy of the flange thickness is barely affected by the eccentricity error. As shown in Table 5, the QR value measurement results are also improved after error correction. The mean error and maximum error of the QR value are both larger than the flange height because it takes more reference points to calculate the QR value, which causes accumulated error.

The standard deviations of the six measurements of each wheel after correction were analyzed and are shown in Fig. 16. The red line in the figure represents the error bars of the six measurements. The maximum standard deviations of the flange height, flange thickness and QR value are 0.11 mm, 0.07 mm and 0.18 mm, respectively, which indicates that the system has good robustness.

In summary, the proposed correction method can effectively reduce the measurement error caused by different wheel diameters, especially for the flange height and QR value. After correction, the reliability and repeatability of the system were significantly improved for different wheels.

VI. CONCLUSION

The online measurement of wheel tread geometric parameters is an important guarantee for the safe operation of trains. To improve the accuracy and reliability of field measurements, an on-site wheel tread geometric parameter detection system based on a line-structured light vision sensor was

proposed in this paper. To achieve good performance in accuracy and precision, we mainly focus on the following two aspects of work in this paper: (1) A subpixel laser stripe centre extraction algorithm based on skeleton extraction was proposed to reduce the interference of a complex lighting environment in the field and improve the extraction accuracy. (2) In order to further improve the measurement accuracy and stability, the influence of the eccentricity error caused by the dynamic measurement on the results was analyzed, a mathematical model was established, and the deformed profile was corrected. The sensor system has been installed on the railway site for dynamic on-line detection of wheel tread geometric parameters. Field tests of real train wheels were conducted, and the effectiveness of the error correction was verified by the measurement results. The sensor system has the advantages of great accuracy, good reliability and fast response speed, making it suitable for on-site measurement of wheel tread profiles.

REFERENCES

[1] J. Luo, F. Xue, and Q. Peng, "Theoretical analysis of railway transportation sustainable development," in *Proc. Int. Conf. Transp. Eng.*, Chengdu, China, 2009, pp. 1890–1895.

[2] L. Liu, F. Zhou, and Y. He, "Automated visual inspection system for bogie block key under complex freight train environment," *IEEE Trans. Instrum. Meas.*, vol. 65, no. 1, pp. 2–14, Jan. 2016.

[3] C. Wang, C. Shen, Q. He, A. Zhang, F. Liu, and F. Kong, "Wayside acoustic defective bearing detection based on improved dopplerlet transform and Doppler transient matching," *Appl. Acoust.*, vol. 101, pp. 141–155, Jan. 2016.

[4] H. Zhang, S. Lu, Q. He, and F. Kong, "Multi-bearing defect detection with trackside acoustic signal based on a pseudo time–frequency analysis and dopplerlet filter," *Mech. Syst. Signal Process.*, vols. 70–71, pp. 176–200, Mar. 2016.

[5] H. J. Yoon, M. J. Park, J. S. Kim, and J. J. Park, "Design of railway journal box embedded with FBG sensor to monitor temperature and acoustic emission signal," *Adv. Mater. Res.*, vol. 566, pp. 480–483, Sep. 2012.

[6] S. Lu and Z. Liu, "Automatic visual inspection of a missing split pin in the China railway high-speed," *Appl. Opt.*, vol. 55, no. 30, pp. 8395–8405, Oct. 2016.

[7] Z. Yao, D. He, Y. Chen, B. Liu, J. Miao, J. Deng, and S. Shan, "Inspection of exterior substance on high-speed train bottom based on improved deep learning method," *Measurement*, vol. 163, Oct. 2020, Art. no. 108013.

[8] S. Zheng, X. Chai, X. An, and L. Li, "Railway track gauge inspection method based on computer vision," in *Proc. IEEE Int. Conf. Mechatronics Autom.*, Chengdu, China, Aug. 2012, pp. 1292–1296.

[9] Y. G. Li, C. L. Li, and L. Z. Li, "The Study on the disease edge detection eechnology of pantograph carbon contact strip," *China Railway*, no. 6, pp. 76–81, Jun. 2018.

[10] J. Pombo, J. Ambrósio, M. Pereira, R. Lewis, R. Dwyer-Joyce, C. Ariaudo, and N. Kuka, "A study on wear evaluation of railway wheels based on multibody dynamics and wear computation," *Multibody Syst. Dyn.*, vol. 24, no. 3, pp. 347–366, Oct. 2010.

[11] J. C. Ji, S. Y. Shao, and Q. B. Feng, "A novel method to measure flange thickness and rim width of wheel sets on line," *Appl. Mech. Mater.*, vol. 330, pp. 237–241, Jun. 2013.

[12] H. He, S. Shao, and Q. Feng, "Online measurement for geometrical parameters based on 2D laser sensor," in *Proc. 9th Int. Symp. Precis. Eng. Meas. Instrum.*, Mar. 2015, Art. no. 944609.

[13] D. Cui, L. Li, H. Wang, Z. Wen, and J. Xiong, "High-speed EMU wheel re-profiling threshold for complex wear forms from dynamics viewpoint," *Wear*, vols. 338–339, pp. 307–315, Sep. 2015.

[14] G. Yun Tian, D. Gledhill, and D. Taylor, "Comprehensive interest points based imaging mosaic," *Pattern Recognit. Lett.*, vol. 24, nos. 9–10, pp. 1171–1179, Jun. 2003.

[15] X. Chen, G. Tian, J. Wu, C. Tang, and K. Li, "Feature-based registration for 3D eddy current pulsed thermography," *IEEE Sensors J.*, vol. 19, no. 16, pp. 6998–7004, Aug. 2019.

[16] X. L. Pan Zhen and G. J. Zhang, "On-site reliable wheel size measurement based on multisensor data fusion," *IEEE Trans. Instrum. Meas.*, vol. 68, no. 3, pp. 4575–4589, Nov. 2019.

[17] Z. Xing, Y. Chen, X. Wang, Y. Qin, and S. Chen, "Online detection system for wheel-set size of rail vehicle based on 2D laser displacement sensors," *Optik*, vol. 127, no. 4, pp. 1695–1702, Feb. 2016.

[18] X. Cheng, Y. Chen, Z. Xing, Y. Li, and Y. Qin, "A novel online detection system for wheelset size in railway transportation," *J. Sensors*, vol. 2016, Apr. 2016, Art. no. 9507213.

[19] X. Chen, J. Sun, Z. Liu, and G. Zhang, "Dynamic tread wear measurement method for train wheels against vibration," *Appl. Opt.*, vol. 54, no. 17, pp. 5270–5280, 2015.

[20] X. Pan, Z. Liu, and G. Zhang, "Reliable and accurate wheel size measurement under highly reflective conditions," *Sensors*, vol. 18, no. 12, p. 4296, Dec. 2018.

[21] H. Soleimani, M. Moavenian, R. Masoudi Nejad, and Z. Liu, "An applied method for railway wheel profile measurements due to wear using image processing techniques," *Social Netw. Appl. Sci.*, vol. 3, no. 2, pp. 1–10, Feb. 2021.

[22] E. J. Bernal, R. M. Martinod, G. R. Betancur, and L. F. Castañeda, "Partial-profilogram reconstruction method to measure the geometric parameters of wheels in dynamic condition," *Vehicle Syst. Dyn.*, vol. 54, no. 5, pp. 606–616, May 2016.

[23] M. Asplund and J. Lin, "Evaluating the measurement capability of a wheel profile measurement system by using GR&R," *Measurement*, vol. 92, pp. 19–27, Oct. 2016.

[24] Z. Lv and Z. Zhang, "Build 3D scanner system based on binocular stereo vision," *J. Comput.*, vol. 7, no. 2, pp. 399–404, Feb. 2012.

[25] L. Jan, J. Fridrich, and M. Goljan, "Detecting digital image forgeries using sensor pattern noise," *Proc. SPIE Int. Soc. Opt. Eng.*, vol. 6072, Feb. 2006, Art. no. 60720Y.

[26] J.-H. Jang and K.-S. Hong, "Detection of curvilinear structures and reconstruction of their regions in gray-scale images," *Pattern Recognit.*, vol. 35, no. 4, pp. 807–824, Apr. 2002.

[27] R. Diversi, R. Guidorzi, and U. Soverini, "Kalman filtering in extended noise environments," *IEEE Trans. Autom. Control*, vol. 50, no. 9, pp. 1396–1402, Sep. 2005.

[28] C. Steger, "Extracting curvilinear structures: A differential geometric approach," in *Computer Vision*. Berlin, Germany: Springer, 1996, pp. 630–641.

[29] F. Li, X. Li, and Z. Liu, "A multi-scale analysis based method for extracting coordinates of laser light stripe centers," *Acta Optica Sin.*, vol. 34, no. 11, pp. 103–108, 2014.

[30] T. Y. Zhang and C. Y. Suen, "A fast parallel algorithm for thinning digital patterns," *Commun. ACM*, vol. 27, no. 3, pp. 236–239, Mar. 1984.

YUNFENG RAN was born in China, in October 1993. He received the B.S. degree from Chongqing University, China, in 2015. He is currently pursuing the Ph.D. degree in optical engineering with Beijing Jiaotong University. His research interest includes photoelectric detection.

QIXIN HE was born in September 1992. He received the B.S. and Ph.D. degrees in optical engineering from Jilin University, China, in 2013 and 2018, respectively. From 2016 to 2018, he was a Visiting Ph.D. Student with Rice University, Houston. Since 2018, he has been serving as a Lecturer with the School of Science, Beijing Jiaotong University. His research interests include optical measurement technology and photoelectric detection technology.

QIBO FENG was born in Hubei, China, in May 1962. He received the B.S. and M.S. degrees from the Hefei University of Technology, China, in 1983 and 1986, respectively, and the Ph.D. degree in optical engineering from Tsinghua University, China, in 1993. Since 1993, he has been serving as an Associate Professor and a Professor with the School of Science, Beijing Jiaotong University. From 1998 to 1999, he was a Visiting Professor with the University of North Carolina, Charlotte. He is currently the Chair Professor and responsible to the disciple of optical engineering. His research interests include optical measurement technology and non-destructive testing.

JIANYING CUI was born in Hebei, China, in February 1964. He received the bachelor's and master's degrees from the Department of Mechanical, Tsinghua University, China, in 1987 and 1989, respectively. Since 1989, he has serving as a Senior Engineer with the School of Science, Beijing Jiaotong University.